

# FSI modeling of the reefed stages and disreefing of the Orion spacecraft parachutes

Kenji Takizawa · Tayfun E. Tezduyar ·  
Cody Boswell · Ryan Kolesar · Kenneth Montel

Received: 13 May 2014 / Accepted: 15 June 2014 / Published online: 18 July 2014  
© Springer-Verlag Berlin Heidelberg 2014

**Abstract** Orion spacecraft main and drogue parachutes are used in multiple stages, starting with a “reefed” stage where a cable along the parachute skirt constrains the diameter to be less than the diameter in the subsequent stage. After a period of time during the descent, the cable is cut and the parachute “disreefs” (i.e. expands) to the next stage. Fluid–structure interaction (FSI) modeling of the reefed stages and disreefing involve computational challenges beyond those in FSI modeling of fully-open spacecraft parachutes. These additional challenges are created by the increased geometric complexities and by the rapid changes in the parachute geometry during disreefing. The computational challenges are further increased because of the added geometric porosity of the latest design of the Orion spacecraft main parachutes. The “windows” created by the removal of panels compound the geometric and flow complexity. That is because the Homogenized Modeling of Geometric Porosity, introduced to deal with the flow through the hundreds of gaps and slits involved in the construction of spacecraft parachutes, cannot accurately model the flow through the windows, which needs to be actually resolved during the FSI computation. In parachute FSI computations, the resolved geometric porosity is significantly more challenging than the modeled geometric porosity, especially in computing the reefed stages and disreefing. Orion spacecraft main and drogue parachutes will both have three stages, with computation of the Stage 1 shape

and disreefing from Stage 1 to Stage 2 for the main parachute being the most challenging because of the lowest “reefing ratio” (the ratio of the reefed skirt diameter to the nominal diameter). We present the special modeling techniques and strategies we devised to address the computational challenges encountered in FSI modeling of the reefed stages and disreefing of the main and drogue parachutes. We report, for a single parachute, FSI computation of both reefed stages and both disreefing events for both the main and drogue parachutes. In the case of the main parachute, we also report, for a 2-parachute cluster, FSI computation of the disreefing from Stage 2 to Stage 3. With results from these computations, we demonstrate that we have to a great extent overcome one of the most formidable challenges in FSI modeling of spacecraft parachutes.

**Keywords** Fluid–structure interaction · Orion spacecraft parachutes · Orion main parachutes · Orion drogue parachutes · Modeled geometric porosity · Resolved geometric porosity · Parachute reefed stages · Parachute disreefing

## 1 Introduction

The Team for Advanced Flow Simulation and Modeling (T★AFSM) has addressed a number of computational challenges encountered in fluid–structure interaction (FSI) modeling of the Orion spacecraft parachutes (see [1,2] and references therein, and [3–6]). These computational challenges include the lightness of the parachute canopy compared to the air masses involved in the parachute dynamics, the geometric porosity created by the hundreds of gaps and slits that the parachute canopy construction includes, and the contact between the parachutes of a cluster, which is how

K. Takizawa (✉)  
Department of Modern Mechanical Engineering, Waseda Institute  
for Advanced Study, Waseda University, 1-6-1 Nishi-Waseda,  
Shinjuku-ku, Tokyo 169-8050, Japan  
e-mail: Kenji.Takizawa@tafsm.org

T. E. Tezduyar · C. Boswell · R. Kolesar · K. Montel  
Mechanical Engineering, Rice University – MS 321, 6100 Main Street,  
Houston, TX 77005, USA  
e-mail: tezduyar@tafsm.org

the Orion spacecraft parachutes will be used. Until recently, these challenges were addressed for the main parachutes and in the incompressible-flow regime, which is where the main parachutes operate. Very recently, the T★AFSM has addressed these challenges for the drogue parachutes (see [7]), in the incompressible-flow regime to a large extent and in the compressible-flow regime to a lesser extent.

The T★AFSM has been addressing the computational challenges with the Stabilized Space–Time FSI (SSTFSI) method [8], which serves as the core numerical technology and is evolving, and special techniques targeting parachute FSI, which were developed in conjunction with the SSTFSI method (see [1,2] and references therein, and [3–6]). The SSTFSI method originated from the Deforming-Spatial-Domain/Stabilized ST (DSD/SST) method [9–12] and its new versions [8,13,14]. Its stabilization components are the Streamline-Upwind/Petrov-Galerkin (SUPG) [15] and Pressure-Stabilizing/Petrov-Galerkin (PSPG) [9,16] methods. As a general-purpose moving-mesh (interface-tracking) method for flows with moving interfaces, the DSD/SST method is comparable to the Arbitrary Lagrangian–Eulerian (ALE) finite element formulation [17], which is of course far more commonly used (see, for example, [2,18–55]).

Special FSI techniques targeting the Orion spacecraft parachutes started in [56,57] and continued in [1,3–6,58–61]. These special FSI techniques, together with the core FSI method, made the T★AFSM the first to bring accurate solution and analysis to ringsail spacecraft parachutes at full scale and to clusters of those parachutes.

Orion spacecraft main and drogue parachutes are used in multiple stages. A “reefed” stage is where a cable along the parachute skirt constrains the diameter to be less than the diameter in the subsequent stage. After a period of time during the descent at the reefed stage, the cable is cut and the parachute “disreefs” (i.e. expands) to the next stage. The reefed stages and disreefing make FSI modeling substantially more challenging than the FSI modeling of fully-open spacecraft parachutes. The additional challenges are created mainly by the increased geometric complexities of the reefed stages and to some extent by the rapid changes in the parachute geometry during disreefing. Orion spacecraft main and drogue parachutes will both have three stages, with computation of the Stage 1 shape and disreefing from Stage 1 to Stage 2 for the main parachute being the most challenging because of the lowest “reefing ratio” (the ratio of the reefed skirt diameter to the nominal diameter).

In the latest design of the Orion spacecraft main parachutes, Sail 11 is removed for every 5th gore to create “windows,” and approximately the top 25 % of Sail 6 is removed for all the gores to create wider gaps (see [1,2,56,57] for the parachute terminology, including “sail,” “gore” and “gap”). The objective is to enhance the stability aspect of the aerodynamic performance of the parachute. We use the acronym

“MP” to identify the parachute with such “modified geometric porosity,” and the acronym “PA” for the parachute with all its sails in place. In FSI modeling of the MP parachute, the flow through the windows creates an additional challenge even for the fully-open parachutes. That is because the Homogenized Modeling of Geometric Porosity (HMGP), first introduced in [56,57] (and then improved in [4,59]) to deal with the flow through the hundreds of gaps and slits of spacecraft parachutes, cannot accurately model the flow through the windows. That flow needs to be actually resolved. This challenge was addressed recently for fully-open spacecraft parachutes—for a single MP parachute in [4] and for a cluster of MP parachutes in [6].

In [4], FSI modeling of the disreefing of a single PA parachute from Stage 2 to Stage 3 was reported, together with a preliminary FSI modeling of a single MP parachute at Stage 2. In this paper, we present the special modeling techniques and strategies we devised to more comprehensively address the computational challenges encountered in FSI modeling of the reefed stages and disreefing of the MP and drogue parachutes. In the case of the MP parachute, the challenges associated with the reefed stages and disreefing are compounded by the challenges associated with the need to resolve the flow through the windows. We report, for a single parachute, FSI computation of both reefed stages and both disreefing events for both the MP and drogue parachutes. In the case of the MP parachute, we also report, for a 2-parachute cluster, FSI computation of the disreefing from Stage 2 to Stage 3.

In the fluid mechanics part, we use the Navier–Stokes equations of incompressible flows. In the structural mechanics part, we use membrane and cable models, under the assumption of large displacements and small strains.

The modeling techniques and computations are presented for a single MP parachute in Sect. 2, for a 2-parachute MP cluster in Sect. 3, and for a single drogue parachute in Sect. 4. The concluding remarks are presented in Sect. 5.

## 2 Single MP parachute

### 2.1 Problem setup

The parachute has three stages: fully reefed (Stage 1), partially reefed (Stage 2), and fully open (Stage 3). The two reefed configurations (Stages 1 and 2) are characterized by a reefing ratio  $\tau_{\text{REEF}} = D_{\text{REEF}}/D_0$ , where  $D_{\text{REEF}}$  is the reefed skirt diameter, and  $D_0$  is the nominal diameter. Stage 1 has  $\tau_{\text{REEF}} = 10\%$  and Stage 2 has  $\tau_{\text{REEF}} = 16\%$ .

All computations are carried out using air properties at standard sea-level conditions. The density is  $2.38 \times 10^{-3}$  slug/ft<sup>3</sup> and the kinematic viscosity is  $1.57 \times 10^{-4}$  ft<sup>2</sup>/s. The material properties of all cables and fabrics on the main parachute were obtained from NASA.



**Fig. 1** MP parachute

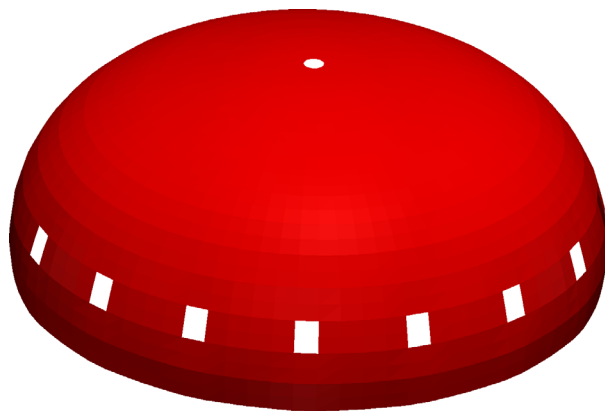
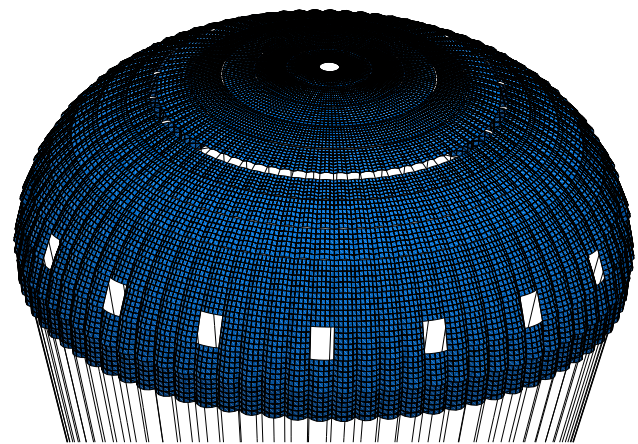


**Fig. 2** Fluid interface for the MP parachute

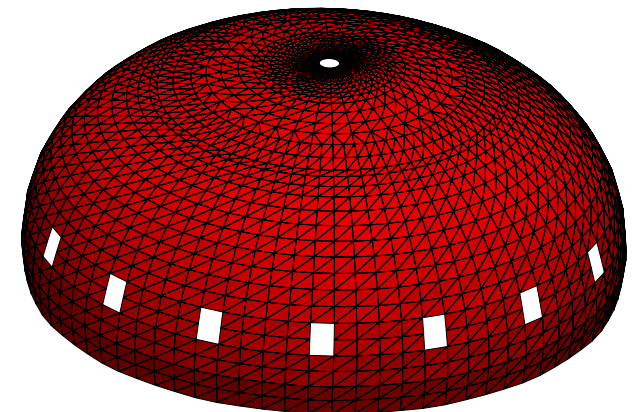


**Fig. 3** Structural mechanics mesh (*top*) and fluid-interface mesh (*bottom*) for the MP parachute. For the number of nodes and elements in these meshes, see Table 1

### 2.2 Description of the parachute

The parachute model is the same as the MP parachute model in [4]. It is a 120 ft ringsail parachute with 4 rings and 9 sails. It is missing panels on every 5th gore on Sail 11 as well as the top 25 % of Sail 6. It has a suspension-line to nominal diameter ratio of  $L_s/D_o = 1.44$ . The payload mass is about 6,900 lbs. Figure 1 shows the MP parachute.

### 2.3 Fluid interface

The fluid-interface model for the MP parachute, shown in Fig. 2, contains gaps where the top vent and missing panels are located. Fluid nodes are placed across these gaps so that flow can be resolved through them. Elsewhere, flow through the canopy due to geometric and fabric porosity is modeled using the HMGP-FGR technique (described in [4]). The fluid-interface model used in [4] differs from the current model in that it has a gap also where the top 25 % of Sail 6 is missing. We model the flow through this gap with HMGP because it results in a more robust interface model for the highly dynamic conditions of disreefing.

*Remark 1* A Stage 2 MP parachute shape was found in [4]. However, we are not able to use that shape and fluid-interface mesh here because of the lack of robustness in the computations in trying to resolve the flow through the gap between Sails 5 and 6. Therefore, we use the fluid-interface mesh described in Sect. 2.3.

### 2.4 Computational methods and parameters

#### 2.4.1 Meshes

The structure and fluid-interface meshes are shown in Fig. 3. The number of nodes and elements for those meshes are given Table 1. The fluid mechanics volume mesh consists of four-node tetrahedral elements, and the membrane elements used in the parachute structure are quadrilateral. The computational domain is box-shaped, with dimensions 1,740 ft × 1,740 ft × 1,566 ft. In order to deal with contact more effectively, two layers of equal-thickness elements are generated in both directions from the fluid interface. The addition of these elements, from our computational experience,

**Table 1** Number of nodes ( $nn$ ) and elements ( $ne$ ) in the structural mechanics and fluid-interface meshes for the single MP parachute. The payload is modeled as a single point-mass element. The cable elements include 1 riser element and 20 elements per suspension line

Structure		
	$nn$	29,714
Membrane	$ne$	24,880
Cable	$ne$	12,161
Interface	$nn$	28,192
Fluid		
Interface	$nn$	2,220
	$ne$	4,276

**Table 2** Number of nodes ( $nn$ ) and elements ( $ne$ ) in the fluid-volume meshes used in Stages 1 and 2

	Mesh 1	Mesh 2
Stage 1		
$nn$	183,974	181,492
$ne$	1,070,764	1,055,401
Stage 2		
$nn$	178,442	177,153
$ne$	1,037,214	1,029,197

makes dealing with contact more robust. The data for the fluid mechanics volume meshes is in Table 2.

The reference frame is moved with a vertical velocity of  $U_{\text{ref}}$ , and the mesh translates horizontally and vertically with the average displacement rate of the structure beyond the reference velocity  $U_{\text{ref}}$ . Here  $U_{\text{ref}}$  is set to a value suitable for the stage computed. We use the velocity form of the free-stream conditions at the lateral boundaries as well since the mesh translates horizontally.

#### 2.4.2 Structural mechanics computations

In the stand-alone structural mechanics computations we have a time-step size of 0.0232 s, 4 nonlinear iterations per time step, and 120 GMRES iterations per nonlinear iteration. In the temporal discretization, we use the generalized- $\alpha$  method [62]. The parameters we use with the method, in the notation of [2], are  $\alpha_m = 1$ ,  $\alpha_f = 1$ ,  $\gamma = 0.9$ , and  $\beta = 0.49$ .

#### 2.4.3 Fluid mechanics computations

The fluid mechanics computations with fixed shapes and positions are done in two parts. The first part is to develop the flow field, and the second part is to have a transition to the FSI computation. In the first part we use the semi-discrete formulation given in [12]. We compute 1,000 time steps with a time-step size of 0.232 s and 6 nonlinear iterations. We note



**Fig. 4** Single MP parachute during Stage 1 to 2 disreef at 0.5 s intervals

that we determine the time-step size for the fluid mechanics computations typically based on Courant number considerations. The number of GMRES iterations per nonlinear iteration is 90. There is no porosity model in this part.

In the second part we use the DSD/SST-TIP1 technique [8], with the SUPG test function option WTSA (see Remark 2 in [8]). The stabilization parameters used are those given in [8] by Eqs. (9)–(12), (14)–(15) and (17), with the  $\tau_{\text{SUGN2}}$  term dropped from Eq. (14). We compute 300 time steps with a time-step size of 0.01 s, 6 nonlinear iterations per time step, and 90 GMRES iterations per nonlinear iteration. The porosity model is HMGP-FGR.

#### 2.4.4 FSI computations

The fully-discretized, coupled fluid and structural mechanics and mesh-moving equations are solved with the quasi-direct coupling technique (see Sect. 5.2 in [8]). We use the SSTFSI-TIP1 technique (see Remarks 5 and 10 in [8]), with the same SUPG test function option and stabilization parameters as those described in Sect. 2.4.3. The structural mechanics time integration method is the same as it is in Sect. 2.4.2.

The Surface-Edge-Node Contact Tracking (SENCT-FC) model and the edge-based contact algorithm described in [59]





**Fig. 5** Single MP parachute maximum principal fabric stress (lb/in<sup>2</sup>) during Stage 1 to 2 disreef at 0.5 s intervals

are used during the disreefing computations. The time-step size is 0.01 s, with 6 nonlinear iterations per time step. The number of GMRES iterations per nonlinear iteration is 120 for the fluid+structure block, and 30 for the mesh-moving block. We use selective scaling (see [8]), with the scale for the structure part set to 10<sup>3</sup> in Stage 1 to 2 disreef and 10<sup>4</sup> in Stage 2 to 3 disreef, for the momentum conservation block of the fluid part set to 10, and for the other parts set to 1.

## 2.5 Disreef computations

### 2.5.1 Stage 1 to 2

The Stage 1 reefed shape is obtained in an FSI computation by starting with a PA parachute shape at Stage 2, described in [4]. This parachute is then reefed to  $\tau_{\text{REEF}} = 10\%$  in a symmetric FSI computation over 300 time steps, where the reefing-line elements, in the reference configuration, are changed from their unstressed lengths to lengths that correspond to  $\tau_{\text{REEF}} = 10\%$ . We note that all reefing and disreefing operations on the reefing-line lengths are performed in the

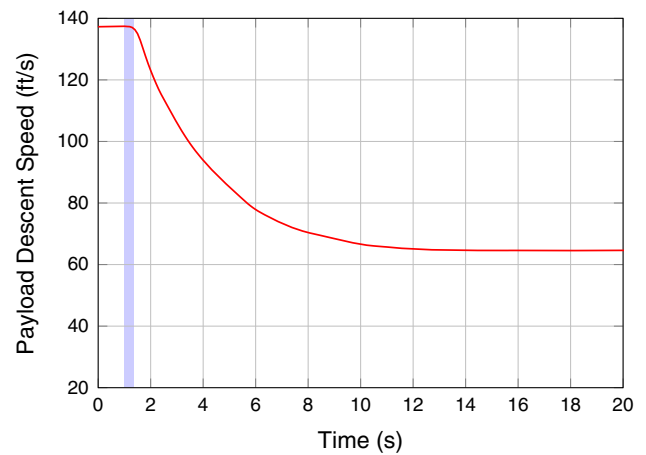


**Fig. 6** Payload descent speed for the single MP parachute during Stage 1 to 2 disreef

reference configuration. The displacements of the PA are then projected to an MP parachute model using a least-squares projection. With this MP shape, we generate a fluid-volume mesh (Mesh 1) that we describe in Table 2 and use that in computing the flow field, as we describe in Sect. 2.4.3. This solution is then used as our starting condition for a symmetric FSI computation, which is computed for 60 s to obtain a settled Stage 1 shape and flow field. Here, as part of the interface projection technique, we use the standard, vector stress projection method instead of the separated stress projection (SSP) [56]. The homogenization model is HMGP-FGR. The descent velocity settles at 137 ft/s and the corresponding stagnation pressure is 22.3 lb/ft<sup>2</sup>.

The Stage 1 to 2 disreef is simulated, in symmetric FSI, by changing the reefing line from  $\tau_{\text{REEF}} = 10\text{--}16\%$  over 35 time steps. After that the reefing line is kept at  $\tau_{\text{REEF}} = 16\%$ . The interface projection method is switched to SSP after 150 time steps of disreefing and stays that way for the remaining computations. At this same instant we remesh, and the fluid-volume mesh becomes Mesh 2.

### 2.5.2 Stage 2 to 3

A structural mechanics computation is first performed for the MP parachute to obtain a starting shape, using the parameters described in Sect. 2.4.2. A uniform stagnation pressure of 0.74 lb/ft<sup>2</sup>, which corresponds to a descent velocity of 25 ft/s, is applied to the unstressed structure and the computation is carried out for 1,000 time steps, reaching a settled shape. Next, a fluid-volume mesh is generated to compute a developed flow field, using the procedures outlined in Sect. 2.4.3. Then, a symmetric FSI computation is performed, over 900 time steps, where the reefing line is shortened to  $\tau_{\text{REEF}} = 16\%$  to obtain the Stage 2 shape. During the reefing, we remesh after each 300 time steps. The final

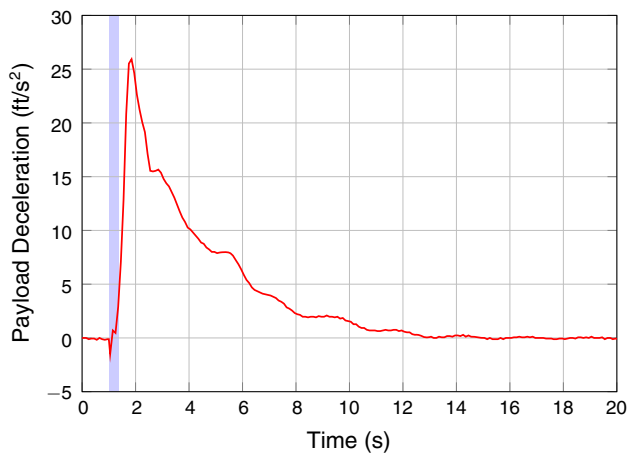


**Fig. 7** Payload deceleration for the single MP parachute during Stage 1 to 2 disreef

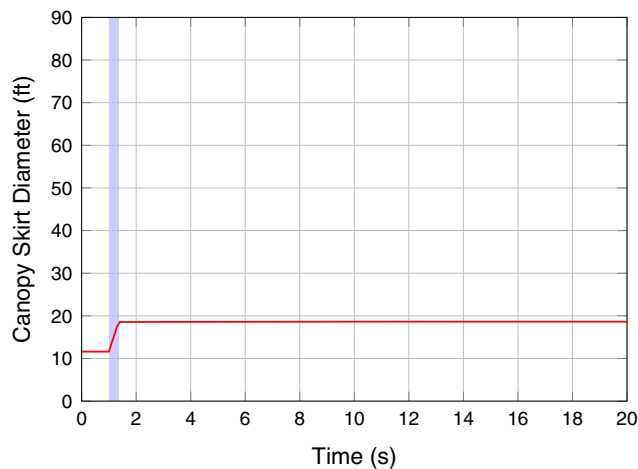


**Fig. 8** Canopy skirt diameter for the single MP parachute during Stage 1 to 2 disreef. The diameter is calculated from the area enveloped by the reefing line

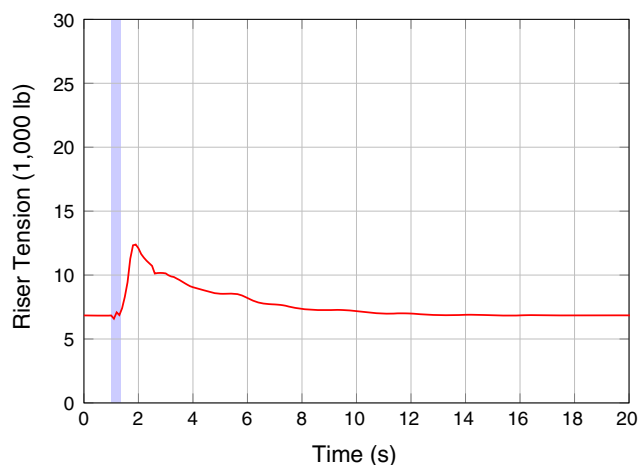


**Fig. 9** Riser tension for the single MP parachute during Stage 1 to 2 disreef



**Fig. 10** Single MP parachute during Stage 2 to 3 disreef at 0.5 s intervals

mesh is Mesh 1 in Table 2. We compute 45 s to reach a settled solution, at which time the descent speed is 65 ft/s and the corresponding stagnation pressure is 5.0 lb/ft<sup>2</sup>.

In disreefing from Stage 2 to 3, the reefing line is instantly set to full length to simulate reefing-line cutting. We remesh 80 time steps after disreefing and use that mesh (Mesh 2) for the remaining 1,820 time steps. The homogenization model is HMGP for 1,000 time steps after disreefing, and HMGP-FGR for the remaining computation.

## 2.6 Results

### 2.6.1 Stage 1 to 2

Figure 4 shows the parachute at 6 instants during the Stage 1 to 2 disreef. The fabric stress is shown in Fig. 5. The payload descent speed, shown in Fig. 6, is a good qualitative match to experimental NASA drop test data. In Fig. 6 and in the three subsequent plots (Figs. 7, 8 and 9),  $t = 0$  corresponds to 100 time steps prior to disreefing. Disreefing starts at  $t = 1.0$  s, ends at  $t = 1.35$  s, and remeshing takes place at  $t = 2.5$  s. The disreefing period is highlighted in blue. The payload deceleration, canopy skirt diameter and riser tension can be seen in Figs. 7, 8 and 9. The descent speed rapidly decreases,

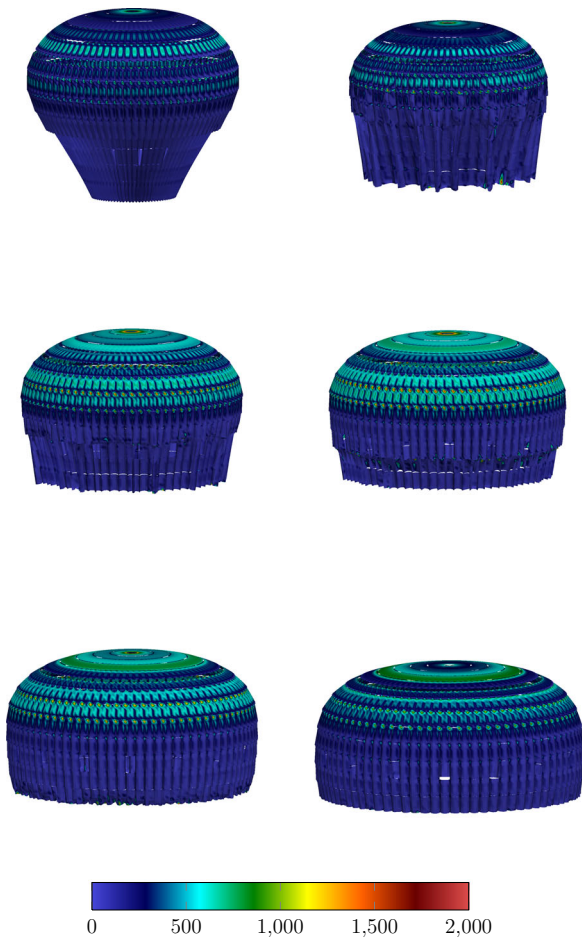


**Fig. 11** Single MP parachute maximum principal fabric stress (lb/in<sup>2</sup>) during Stage 2 to 3 disreef at 0.5 s intervals

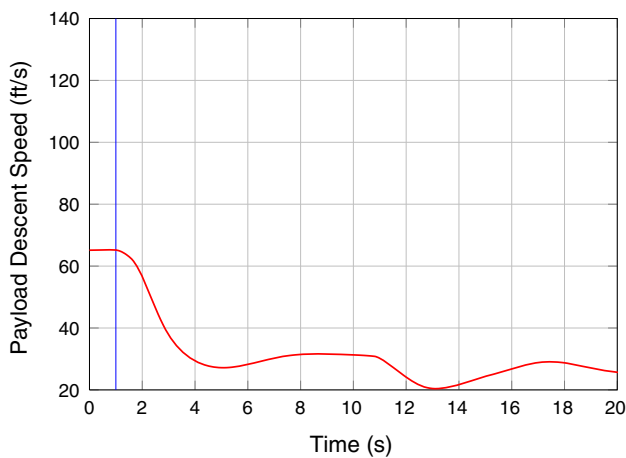


**Fig. 12** Payload descent speed for the single MP parachute during Stage 2 to 3 disreef

and then begins to steady out before it reaches its settled Stage 2 value. This is important for the disreef because it means the parachute does not over-inflate and smoothly transitions to its next stage of flight.

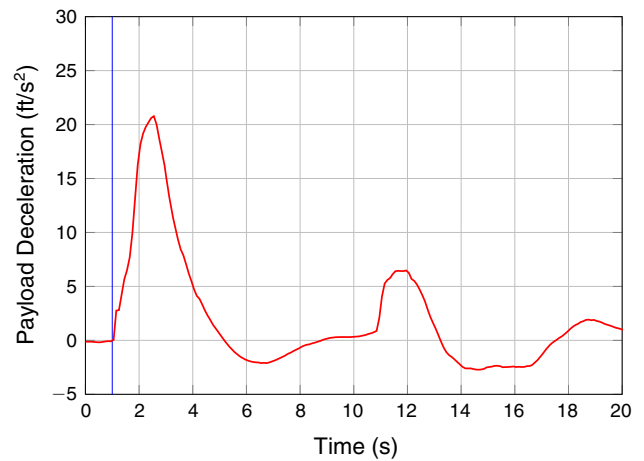


**Fig. 13** Payload deceleration for the single MP parachute during Stage 2 to 3 disreef

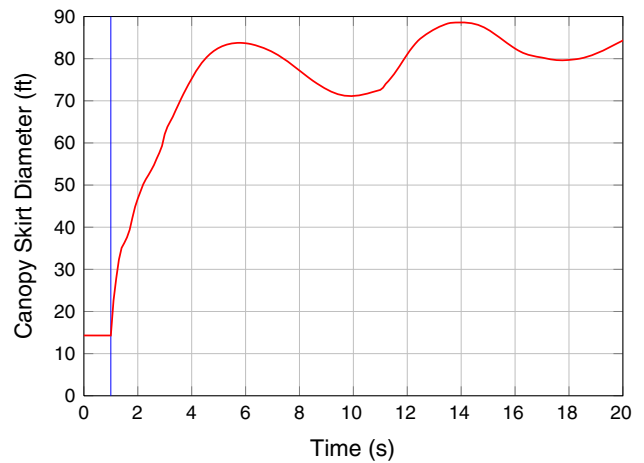


**Fig. 14** Canopy skirt diameter for the single MP parachute during Stage 2 to 3 disreef

### 2.6.2 Stage 2 to 3

Figures 10 and 11 show the parachute and the fabric stress during the Stage 2 to 3 disreef. Figure 12 shows the payload descent speed. In that figure, and in the three subsequent plots (Figs. 13, 14 and 15),  $t = 0$  corresponds to 100 time steps prior to disreefing. Disreefing happens at  $t = 1.0$  s, and remeshing takes place at  $t = 1.8$  s. The blue vertical line marks the disreefing instant. The payload deceleration, canopy skirt diameter and riser tension can be seen in Figs. 13, 14 and 15. The Stage 2 to 3 disreef follows a similar qualitative trend as the Stage 1 to 2 disreef. The Stage 2 to 3 disreef exhibits greater peak loading on the riser, however the fabric stress is smaller on the canopy. After the parachute is fully inflated to Stage 3, it begins a breathing motion.

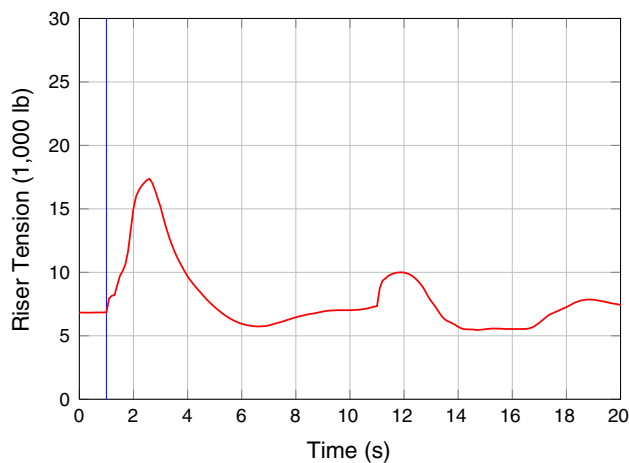


**Fig. 15** Riser tension for the single MP parachute during Stage 2 to 3 disreef

### 3 2-Parachute MP cluster

#### 3.1 Problem setup

Here, a 2-parachute (2P) cluster disreefing from Stage 2 to 3 is presented. Each parachute has  $\tau_{\text{REEF}} = 16\%$  at Stage 2, and the reefing line is cut instantly. The payload mass is about 20,000 lbs. The air properties are the same as those given in Sect. 2.1. The cluster of Stage 2 parachutes is assumed to be settled in a steady-state shape.

#### 3.2 Computational methods and parameters

The structure and fluid-interface models are the same as those used for the single MP parachute. The Stage 2 shape for each of the two parachutes is acquired by using the settled Stage 2 shape of the single MP parachute from Sect. 2.

##### 3.2.1 Meshes

The structural mechanics and fluid-interface meshes for the 2P cluster are generated by combining two single-MP meshes with an angle of  $5^\circ$  between the two parachute axes. See Table 3 for the number of nodes and elements for the structure and fluid-interface meshes.

The fluid-domain size is the same as in Sect. 2.4.1. In generating the fluid-volume mesh, again, two layers of equal-thickness elements are created in both directions from the interface. The data for the fluid mechanics volume mesh is in Table 4.

##### 3.2.2 Fluid mechanics and FSI computation

The fluid mechanics and FSI computations are based on the same formulations, test functions, and stabilization parameters as those described in Sects. 2.4.3 and 2.4.4. For the 2P cluster we use SSP as the interface projection technique.

**Table 3** Number of nodes ( $m$ ) and elements ( $ne$ ) in the structural mechanics and fluid-interface meshes for the 2P cluster. The payload is modeled as a single point-mass element. There are two risers consisting of one cable element each, and each suspension line has 20 elements

Structure		
	$nn$	59,427
Membrane	$ne$	74,083
Cable	$ne$	24,322
Interface	$nn$	56,383
Fluid		
Interface	$nn$	4,440

**Table 4** Number of nodes ( $nn$ ) and elements ( $ne$ ) in the fluid-volume meshes used in the 2P cluster computations

	Mesh 1	Mesh 2
$nn$	324,827	327,953
$ne$	1,900,291	1,918,842

The fluid mechanics computation is carried out with the mesh shown in Table 4 (Mesh 1), with the same procedure as described in Sect. 2.4.3. A time-step size of 0.01 s is used, with 6 nonlinear iterations per time step, and 120 GMRES iterations for the fluid+structure block and 30 for the mesh-moving block. The SENCT-FC and edge-based contact models are used. We use selective scaling, with the scale for the structure part set to  $10^4$ , for the momentum conservation block of the fluid part set to 10, and for the other parts set to 1.

#### 3.3 Disreef computations

After computing a developed flow field, which corresponds to a descent speed of 65 ft/s, a full FSI computation is performed. The full FSI computation continues for approximately 45 s to reach a settled descent velocity. The spin removal technique, described in [6], is utilized about every 300 time steps. The HMGP technique is used. The descent velocity settles at 75 ft/s, and the corresponding stagnation pressure is 6.7 lb/ft<sup>2</sup>.

Similar to Sect. 2.5.2, the reefing line is instantly set to full length to simulate reefing-line cutting. We remesh 70 time steps after disreefing, and use that mesh (Mesh 2) for the remaining duration. The homogenization model is HMGP for 1,250 time steps after disreefing, and HMGP-FGR for the remaining computation.

#### 3.4 Results

Figures 16, 17, 18 and 19 show the parachutes during the disreef. The payload descent speed, as shown in Fig. 20, is a





**Fig. 16** 2P cluster at  $t = 0$  s and  $t = 0.5$  s



**Fig. 17** 2P cluster at  $t = 1.0$  s and  $t = 1.5$  s



**Fig. 18** 2P cluster at  $t = 2.0$  s and  $t = 2.5$  s



**Fig. 19** 2P cluster at  $t = 3.0$  s and  $t = 3.5$  s

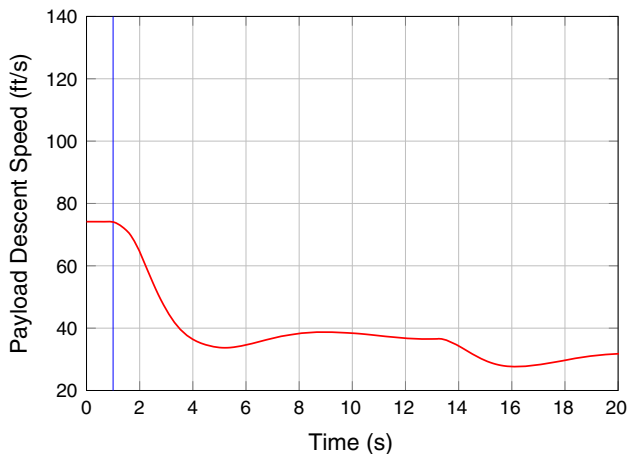


**Fig. 20** Payload descent speed for the 2P cluster

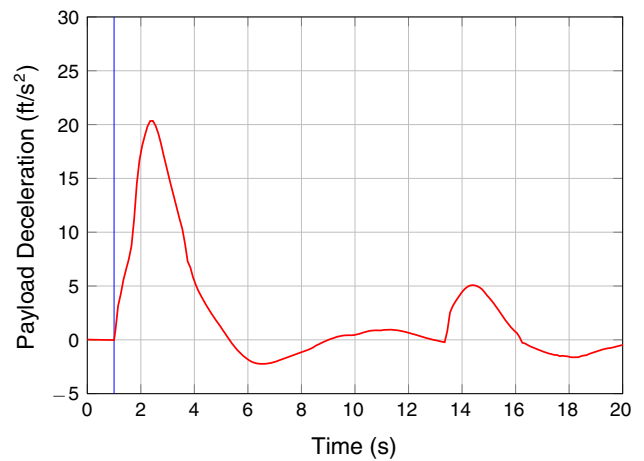


**Fig. 21** Payload deceleration for the 2P cluster

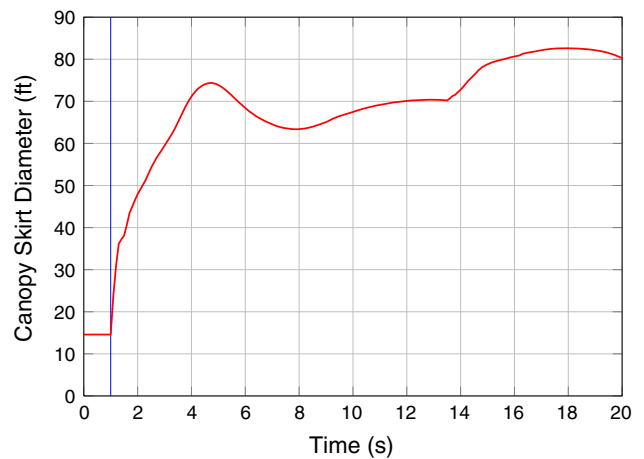


**Fig. 22** Average canopy skirt diameter for the 2P cluster

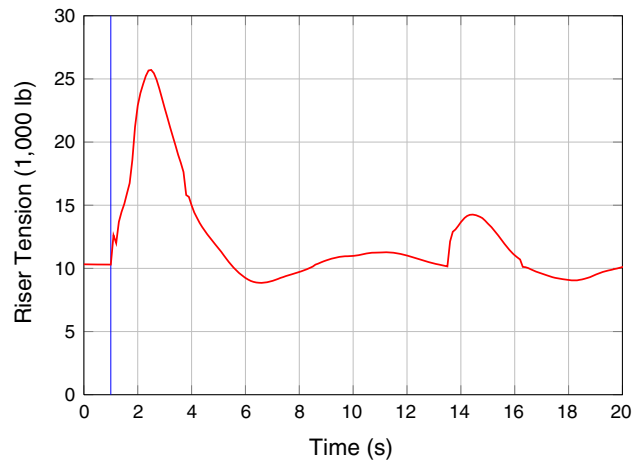


**Fig. 23** Average riser tension for the 2P cluster

good qualitative match to experimental NASA drop test data. In that figure, and in the three subsequent plots (Figs. 21, 22 and 23),  $t = 0$  corresponds to 100 time steps prior to disreef-

ing. Disreefing happens instantly at  $t = 1.0$  s, and remeshing takes place at  $t = 1.7$  s. The blue vertical line marks the disreefing instant.

**Table 5** Standard-day air properties for each FC

FC	Altitude (ft)	Density (slug/ft <sup>3</sup> )	Viscosity (slug/ft s)
1	10,000	0.001756	$3.534 \times 10^{-7}$
2	20,000	0.001267	$3.325 \times 10^{-7}$
3	35,000	0.000738	$2.995 \times 10^{-7}$

The payload deceleration, canopy skirt diameter, and riser tension can be seen in Figs. 21, 22 and 23. The riser tension and diameter are averaged between the two canopies since the data is very similar for each canopy.

## 4 Drogue parachute

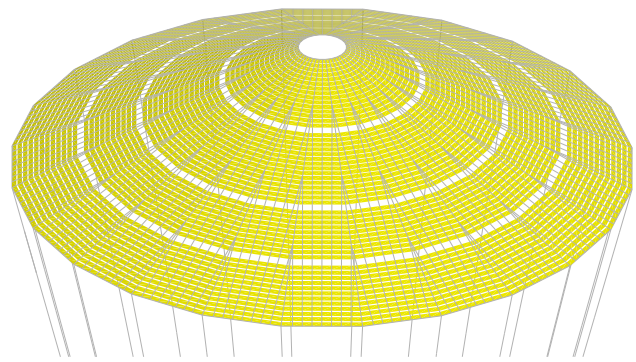
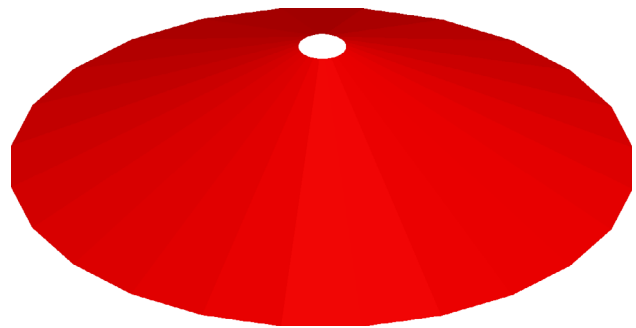
### 4.1 Problem setup

The drogue parachutes have two reefed configurations, just as the main parachutes. Stage 1 has  $\tau_{\text{REEF}} = 38\%$  and Stage 2 has  $\tau_{\text{REEF}} = 49\%$ . The material properties of all cables and fabrics on the drogue were obtained from NASA.

As the drogues are designed to deploy at a wide range of altitudes and speeds, we chose three altitudes to model a single drogue: 10,000, 20,000, and 35,000 ft. These will be referred to as Flight Conditions (FC) 1–3, respectively. Standard-day air properties are assumed at each FC and these properties are in Table 5. The free-stream Mach number is 0.3, allowing the incompressible-flow equations to be used. This descent speed corresponds to a free-stream dynamic pressure of 91.695, 61.310, and 31.454 lb/ft<sup>2</sup> for FC 1–3, respectively.

### 4.2 Description of the parachute

The drogue being modeled is a 23-ft nominal diameter Variable Porosity Conical Ribbon parachute. It has 24 gores, each of which is made up of 52 2-inch horizontal ribbons that are spaced and retained at close intervals by seven vertical tapes. The geometric porosity of the drogue comes from the vent, the gaps between ribbons, and the three larger gaps or “missing ribbons” where ribbons are removed from the otherwise geometrically invariant configuration. These missing ribbons, just like the larger gaps and window in the MP parachute, allow a localized increase in flow that helps prevent the boundary layer from reattaching to the canopy, thereby increasing the stability of the parachute. The suspension-line to nominal diameter ratio,  $L_s/D_0$ , for the drogue is 2. The payload mass is about 10,300 lbs. See Fig. 24 for a model of the drogue parachute.

**Fig. 24** Drogue parachute structure**Fig. 25** Fluid interface for drogue parachute

### 4.3 Fluid interface

The slits between the ribbons are handled with HMGP. Just as the flow is not resolved through the larger gap in the MP parachute, the drogue fluid interface does not have the larger gaps created by the missing ribbons. Therefore, flow is only resolved through the vent of the drogue and HMGP is used elsewhere. Figure 25 shows the drogue fluid interface.

In the drogue FSI computations also we use nonmatching meshes at the fluid–structure interface. The fluid-interface mesh is less refined than the structure mesh, as seen in Fig. 26. This allows the fluid mesh to be more affordable and more manageable for mesh moving. In the radial direction, two ribbons and two slits are covered by one element height in fluid-interface mesh. The larger gaps are covered by one fluid element. In the circumferential direction, the fluid-interface refinement varies along the length of the gore. At the vent, the fluid-interface mesh contains one element per gore. After each missing ribbon, this number increases by one so that the number of elements across a gore at the skirt is four.

Each node on the fluid-interface mesh exactly matches a node on the structure-interface mesh. For Stage 2 and Stage 3 computations, the fluid node location is simply equal to the location of the corresponding structure node for all nodes on the fluid-interface mesh. However, this becomes problematic

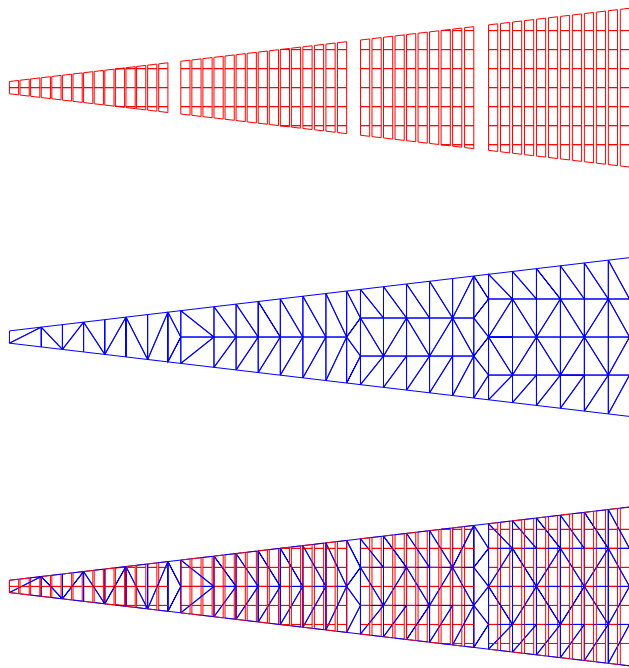


**Fig. 26** Drogue structure interface (*top*), fluid interface (*middle*), and overlay (*bottom*) for a single gore

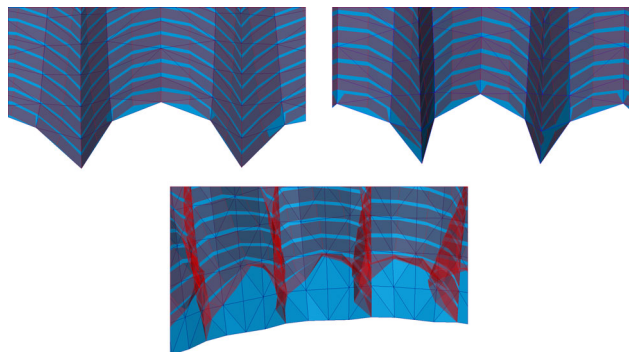


**Fig. 27** Views of the structure (*red*) and fluid-interface (*blue*) meshes near the skirt for Stage 3, Stage 2, and Stage 1

for Stage 1 computations where the membrane elements near the skirt of the structure-interface mesh have a tendency to fold. In order to prevent the fluid elements from tangling at these folding areas, a special version of the FSI-DGST (introduced in [8]) is used. In this technique, the location of fluid nodes along the radials of the drogue are equal to the location of the corresponding structure nodes and the location of all other fluid nodes are linearly interpolated between the two nearest radial nodes that lie on the same circumferential line. Consequently, the shape of the fluid-interface mesh in Stage 1 computations is dependent on only the radials. Figure 27 illustrates the differences in interface projection methods between the various reefed stages.

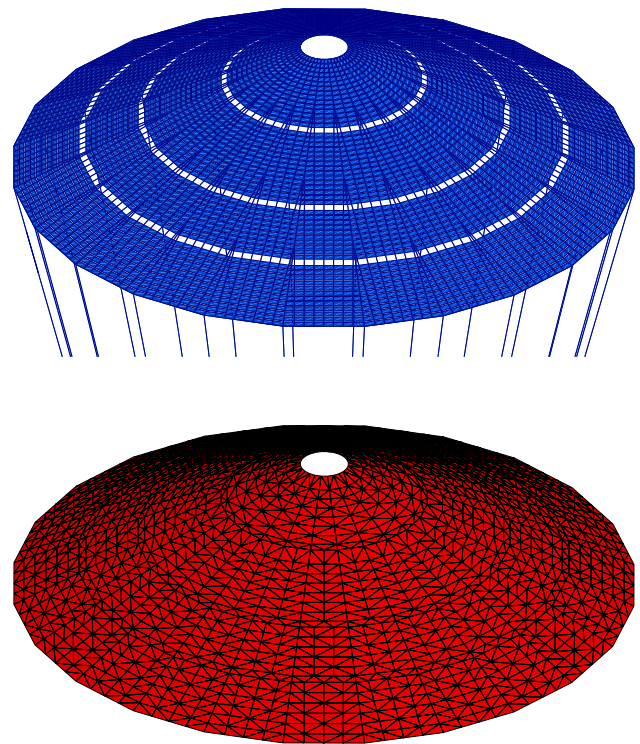


**Fig. 28** Structural mechanics mesh (*top*) and fluid-interface mesh (*bottom*) for the drogue parachute. For the number of nodes and elements in these meshes, see Table 6

**Table 6** Number of nodes ( $m$ ) and elements ( $ne$ ) in the structural mechanics and fluid-interface meshes for the drogue. The cable elements include 1 riser element and 25 elements per suspension line. Also, the payload is modeled as a single point-mass element

Structure		
	$mn$	13,586
Membrane	$ne$	6,576
Cable	$ne$	13,610
Interface	$nn$	13,008
Fluid		
Interface	$mn$	1,680
	$ne$	3,240

#### 4.4 Computational methods and parameters

##### 4.4.1 Meshes

The structure and fluid-interface meshes used during the drogue disreef computations are shown in Fig. 28.

Table 6 shows the number of nodes and elements for those meshes. The fluid mechanics volume mesh consists of four-node tetrahedral elements, and the membrane elements used in the parachute structure are quadrilateral. The computational domain is cylindrical with a radius of 174.4 ft and a height of 310.5 ft. The number of nodes and elements for the

**Table 7** Number of nodes ( $nn$ ) and elements ( $ne$ ) in the fluid-volume meshes

	FC 1	FC 2	FC 3
Stage 3 (Mesh 1)			
$nn$	107,031	107,031	107,031
$ne$	618,490	618,490	618,490
Stage 3 to 1 (Mesh 2)			
$nn$	149,928	146,000	146,599
$ne$	873,938	849,941	853,781
Stage 1 to 2 (Mesh 3)			
$nn$	156,721	153,047	153,446
$ne$	914,213	892,347	894,630
Stage 2 (Mesh 4)			
$nn$	147,787	Same as	Same as
$ne$	860,722	Mesh 2	Mesh 2
Stage 2 to 3 (Mesh 5)			
$nn$	147,674	147,537	147,112
$ne$	860,049	859,373	856,898

fluid-volume meshes used in the computations are given in Table 7.

The reference frame is moved with a vertical velocity of  $U_{\text{ref}}$ , and the mesh translates horizontally and vertically with the average displacement rate of the structure beyond  $U_{\text{ref}}$ . Here,  $U_{\text{ref}}$  is set to the velocity corresponding to Mach 0.3 for all FCs and stages: 323.2, 311.1, and 291.9 ft/s for FC 1–3, respectively. We use the velocity form of the free-stream conditions at the lateral boundaries.

#### 4.4.2 Structural mechanics computations

In the stand-alone structural mechanics computations for the drogue, a time-step size of  $3.56 \times 10^{-3}$  s, 4 nonlinear iterations per time step, 100 GMRES iterations per nonlinear iteration, and a mass-proportional damping coefficient of  $1.41 \times 10^5 \text{ s}^{-1}$  are used. The generalized- $\alpha$  method is used for temporal discretization. The parameters used in this method are  $\alpha_m = 2$ ,  $\alpha_f = 1$ ,  $\gamma = 1.5$ , and  $\beta = 1$ .

#### 4.4.3 Fluid mechanics computations

The fluid mechanics computations with fixed shapes and positions are done in two parts. In the first part, we use the semi-discrete formulation given in [12]. With this formulation, 1,000 time steps are computed with time-step sizes of  $7.12 \times 10^{-3}$ ,  $7.39 \times 10^{-3}$ , and  $7.88 \times 10^{-3}$  s for FC 1–3, respectively, and 6 nonlinear iterations per time step. The number of GMRES iterations per nonlinear iteration is 90. There is no porosity model in this part.

In the second part, we use the DSD/SST-TIP1 technique [8], with the SUPG test function option WTSA (see Remark 2 in [8]). The stabilization parameters used are those given in [8] by Eqs. (9)–(12), (14)–(15) and (17), with the  $\tau_{\text{SUGN2}}$  term dropped from Eq. (14). We compute 1,200 time steps with time-step sizes of  $3.59 \times 10^{-4}$ ,  $3.70 \times 10^{-4}$ , and  $3.94 \times 10^{-4}$  s for FC 1–3, respectively; 6 nonlinear iterations per time step; and 90 GMRES iterations per nonlinear iteration. The porosity model is HMGP.

#### 4.4.4 FSI computations

The fully-discretized, coupled fluid and structural mechanics and mesh-moving equations are solved with the quasi-direct coupling technique (see Sect. 5.2 in [8]). We use the SSTFSI-TIP1 technique (see Remarks 5 and 10 in [8]), with the same SUPG test function option and stabilization parameters as those described in Sect. 4.4.3. For the structural mechanics time integration we again use the generalized- $\alpha$  method, with the parameters  $\alpha_m = 1$ ,  $\alpha_f = 1$ ,  $\gamma = 0.9$ , and  $\beta = 0.49$ .

The SSP technique is used in projecting fluid stresses to the structure. The porosity model is HMGP. No contact models are used for any of the drogue disreefings.

The time-step sizes are  $3.59 \times 10^{-4}$ ,  $3.70 \times 10^{-4}$ , and  $3.94 \times 10^{-4}$  s for FC 1–3, respectively, with 6 nonlinear iterations per time step. The number of GMRES iterations per nonlinear iteration is 90 for the fluid+structure block, and 30 for the mesh-moving block. We use selective scaling, with the scale for the structure part set to  $10^2$  and for the other parts set to 1.

### 4.5 Disreef computations

#### 4.5.1 Initialization

First, a stand-alone structural mechanics computation is performed to obtain an initial inflated shape. A uniform pressure equal to the stagnation pressure at a descent Mach number of 0.3 for 10,000 ft ( $91.697 \text{ lb/ft}^2$ ) is applied to the drogue canopy with the payload fixed. The initial inflated shape is settled after approximately 15,000 time steps.

Next, a fluid mechanics volume mesh (Mesh 1) is generated. Three fluid mechanics computations are performed—one for each flight condition—using the procedures described in Sect. 4.4.3. These results are used as the starting conditions for Stage 3 symmetric FSI computations. The mesh relaxation technique introduced in Sect. 2.2 of [6] is employed when needed during the symmetric FSI computations, thereby allowing Mesh 1 to be used throughout. After carrying out 800 time steps of Stage 3 symmetric FSI computation, the drogue is incrementally reefed in symmetric FSI using a similar approach as in [58]. The length of the reefing-line elements in the drogue structure mesh are gradually (linearly)



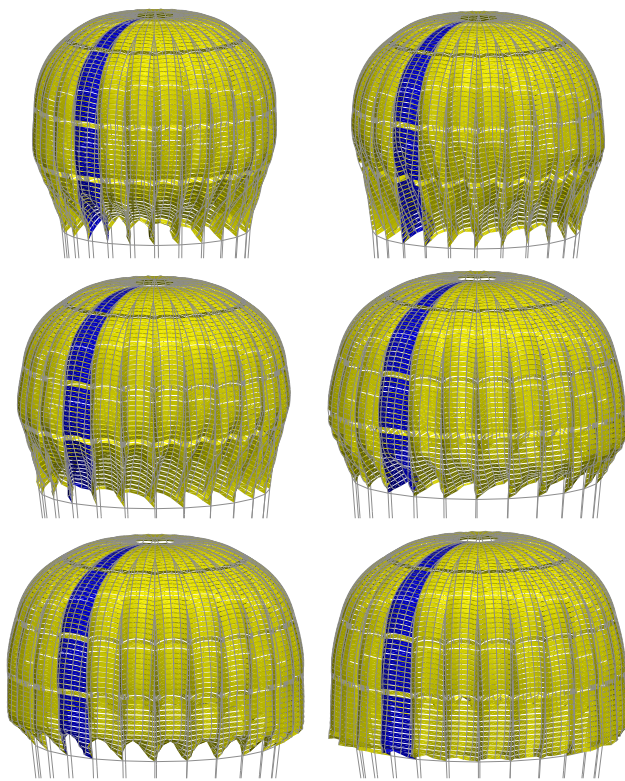


**Fig. 29** Drogue parachute. Structure shape during Stage 1 to 2 disreef (FC 1) at 0.02 s intervals

reduced in three phases. In the first phase, the drogue is reefed to  $\tau_{REEF} = 60\%$  over 300 time steps. In the second phase, it is reefed further to  $\tau_{REEF} = 49\%$  (Stage 2) over 300 time steps. In the third phase, it is reefed to  $\tau_{REEF} = 38\%$  (Stage 1) over 300 time steps. For each of the three flight conditions, the fluid volume is remeshed (to Mesh 2) at one instant during the reefing computation.

The fluid volume resulting from the third phase is remeshed (to Mesh 3) and the interface projection method is switched, as described in Sect. 4.3. A fully-coupled FSI computation is then carried out with this Stage 1 mesh for 9,000 time steps until the shape settles. Similarly, the fluid-volume meshes resulting from the second phase are used as the starting meshes in fully-coupled FSI computations of Stage 2. Before carrying out this computation, the fluid volume is remeshed for FC 1 (to Mesh 4), but not for FC 2 or 3. The interface projection method is not changed for any of the Stage 2 computations. A fully-coupled FSI computation is carried out with these Stage 2 meshes for 9,000 time steps until the shape settles. Afterward, the fluid volume for each of the three flight conditions is remeshed (to Mesh 5) in order to remove the mesh distortion due to the parachute rotating around its riser axis.

The fluid-volume mesh used for the Stage 1 to 2 disreef is Mesh 3, and the one used for the Stage 2 to 3 disreef is Mesh

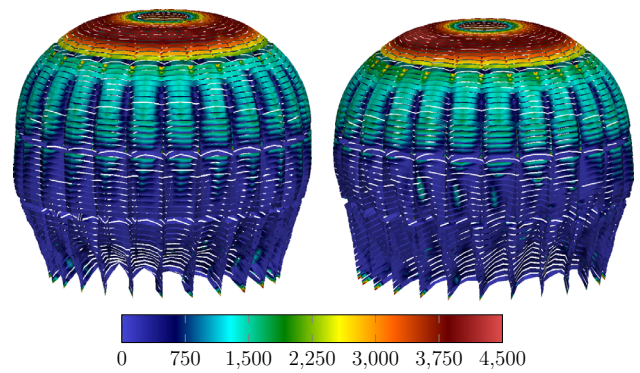


**Fig. 30** Drogue parachute. Maximum principal fabric stress (lb/in<sup>2</sup>) during Stage 1 to 2 disreef (FC 1) at 0 s and 0.02 s

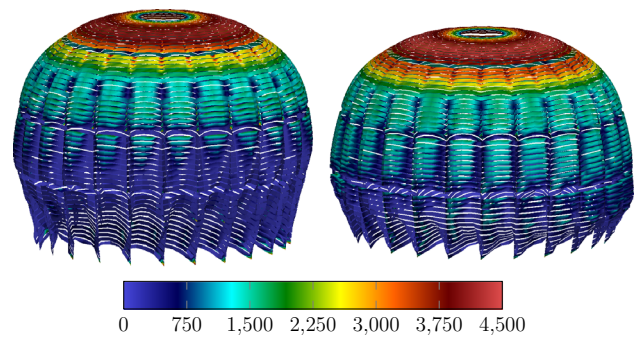


**Fig. 31** Drogue parachute. Maximum principal fabric stress (lb/in<sup>2</sup>) during Stage 1 to 2 disreef (FC 1) at 0.04 s and 0.06 s

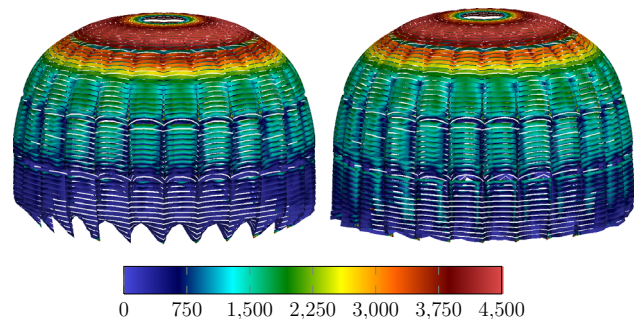


**Fig. 32** Drogue parachute. Maximum principal fabric stress (lb/in<sup>2</sup>) during Stage 1 to 2 disreef (FC 1) at 0.08 s and 0.1 s

5. The number of nodes and elements for these fluid-volume meshes is shown in Table 7. Prior to disreefing, the spinning component of the drogue is removed using the technique described in Sect. 2.1 of [6]. The vertical component of the average velocity (beyond  $U_{ref}$ ) is also removed to ensure that the disreef is being modeled at a starting descent Mach number of exactly 0.3.

#### 4.5.2 Stage 1 to 2

The Stage 1 to 2 disreef is simulated by changing the reefing line from  $\tau_{REEF} = 38\%$  to  $\tau_{REEF} = 49\%$  instantly. This

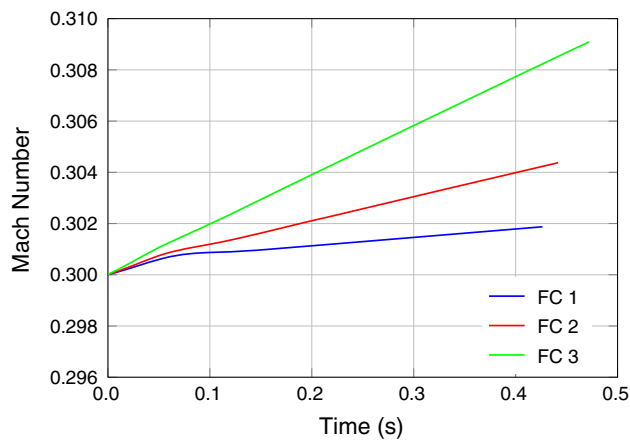


**Fig. 33** Drogue parachute. Payload descent Mach number during Stage 1 to 2 disreef

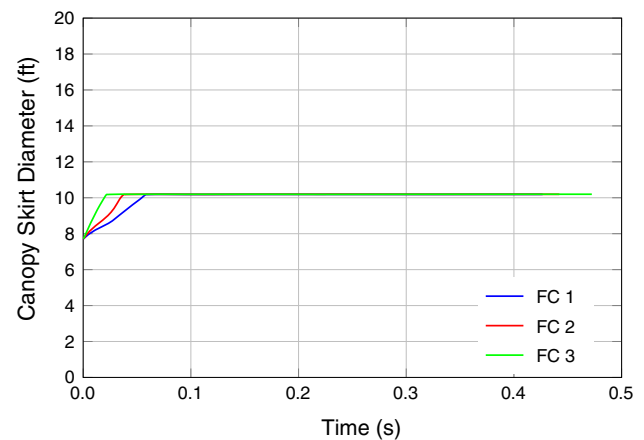


**Fig. 35** Drogue parachute. Canopy skirt diameter during Stage 1 to 2 disreef

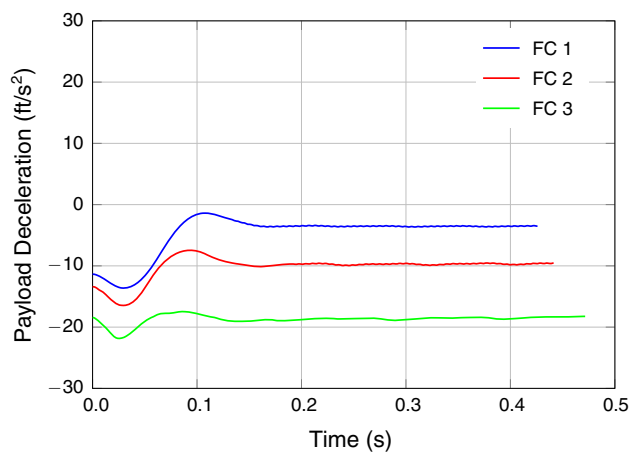


**Fig. 34** Drogue parachute. Payload deceleration during Stage 1 to 2 disreef

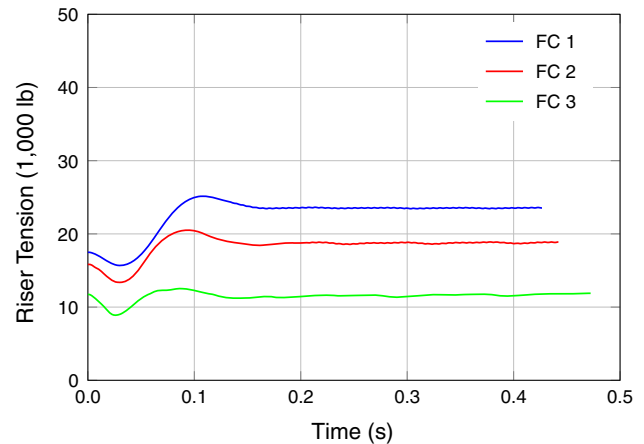


**Fig. 36** Drogue parachute. Riser tension during Stage 1 to 2 disreef

fully-coupled FSI computation is carried out for 1,200 time steps for all flight conditions, using the same parameters as those reported in Sect. 4.4.4.

#### 4.5.3 Stage 2 to 3

To disreef the drogue from Stage 2 to 3, the reefing line is instantly changed from  $\tau_{\text{REEF}} = 49\%$  to full open. The computation is carried out for 668, 733, and 1,200 time steps for FC 1–3, respectively. The parameters used for these fully-coupled FSI computations are the same as those reported in Sect. 4.4.4.

### 4.6 Results

#### 4.6.1 Stage 1 to 2

Figure 29 shows the drogue structure at six instants during the Stage 1 to 2 disreef at FC 1. The fabric stress at these

instants is shown in Figs. 30, 31 and 32. The payload descent Mach number, payload deceleration, canopy skirt diameter, and riser tension, all as a function of time, during the Stage 1 to 2 disreef can be seen in Figs. 33, 34, 35 and 36, respectively.

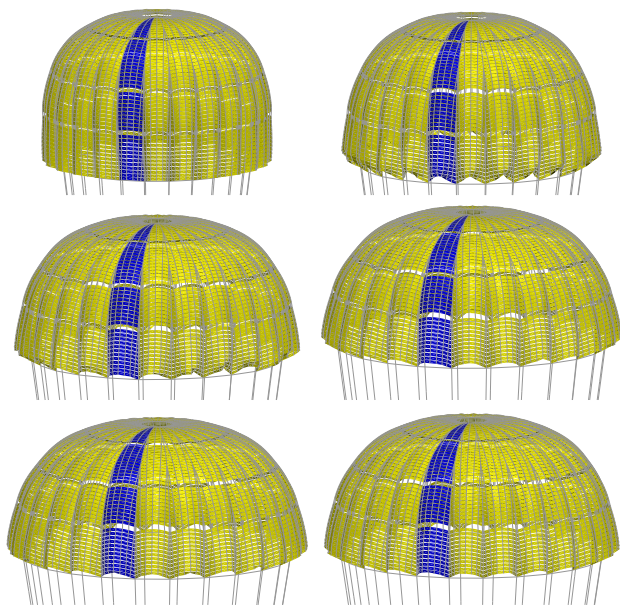
#### 4.6.2 Stage 2 to 3

Figure 37 shows the drogue structure at six instants during the Stage 2 to 3 disreef at FC 1. The fabric stress at these instants is shown in Figs. 38, 39 and 40. The payload descent Mach number, payload deceleration, canopy skirt diameter, and riser tension, all as a function of time, during the Stage 2 to 3 disreef can be seen in Figs. 41, 42, 43 and 44, respectively.

### 5 Concluding remarks

We have presented the special modeling techniques and strategies we devised to address the computational challenges encountered in FSI modeling of the reefed stages and dis-





**Fig. 37** Drogue parachute. Structure shape during Stage 2 to 3 disreef (FC 1) at 0.02 s intervals

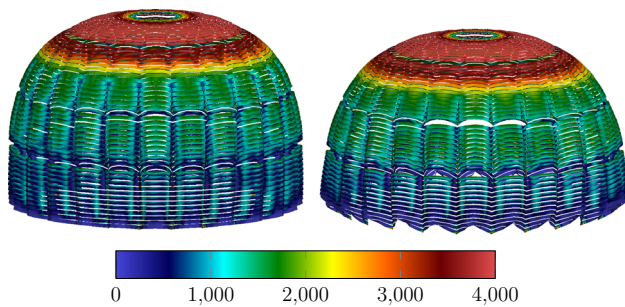


**Fig. 38** Drogue parachute. Maximum principal fabric stress ( $\text{lb}/\text{in}^2$ ) during Stage 2 to 3 disreef (FC 1) at 0 s and 0.02 s

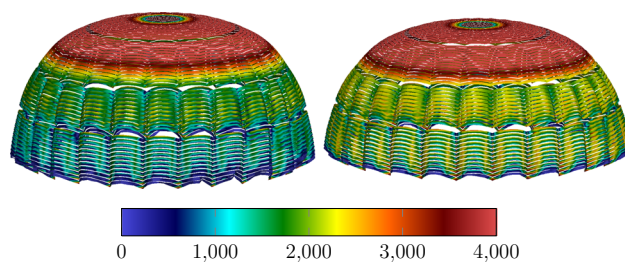


**Fig. 39** Drogue parachute. Maximum principal fabric stress ( $\text{lb}/\text{in}^2$ ) during Stage 2 to 3 disreef (FC 1) at 0.04 s and 0.06 s

reefing of the Orion spacecraft main and drogue parachutes. The reefed stages and disreefing make FSI modeling substantially more challenging than the FSI modeling of fully-open spacecraft parachutes. The additional challenges are created mainly by the increased geometric complexities of the reefed stages and to some extent by the rapid changes in the parachute geometry during disreefing. Orion spacecraft

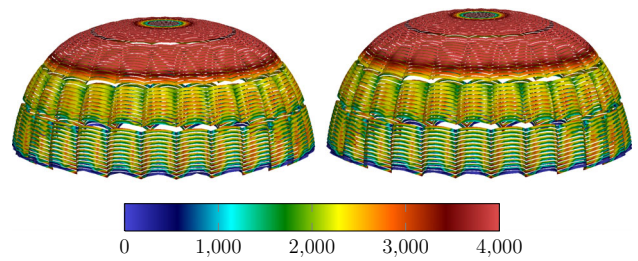


**Fig. 40** Drogue parachute. Maximum principal fabric stress ( $\text{lb}/\text{in}^2$ ) during Stage 2 to 3 disreef (FC 1) at 0.08 s and 0.1 s

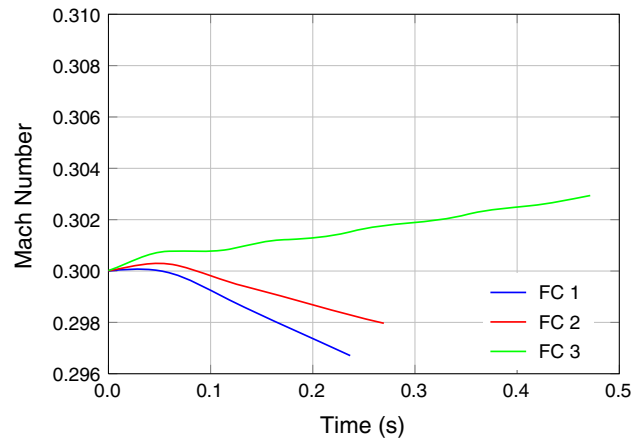


**Fig. 41** Drogue parachute. Payload descent Mach number during Stage 2 to 3 disreef

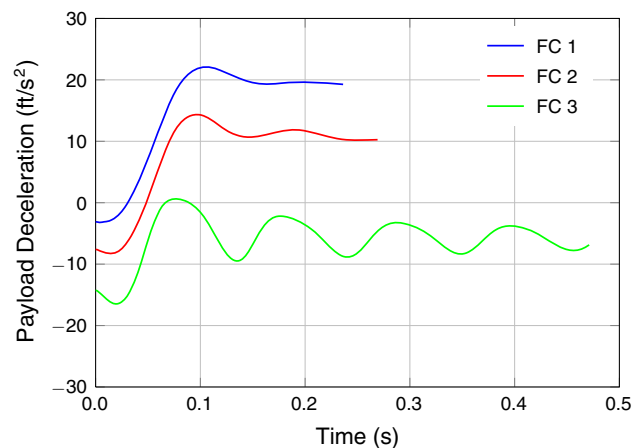


**Fig. 42** Drogue parachute. Payload deceleration during Stage 2 to 3 disreef

main and drogue parachutes will both have three stages, with computation of the Stage 1 shape and disreefing from Stage 1 to Stage 2 for the main parachute being the most challenging because of the lowest reefing ratio. The computational challenges are further increased because of the added geometric porosity of the latest design of the Orion spacecraft main parachutes. This parachute with modified geometric porosity, which we call “MP” parachute in the paper, has

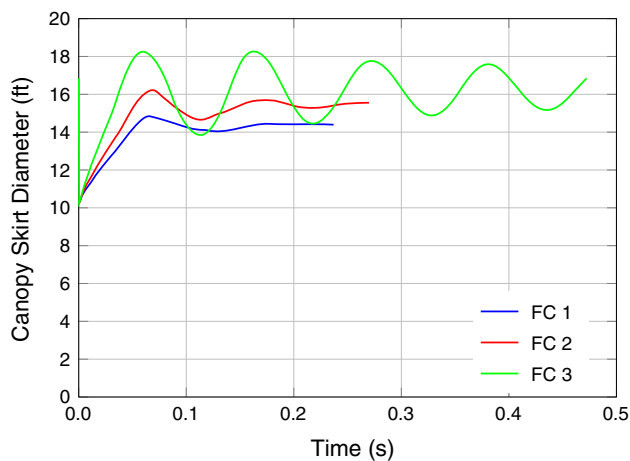


**Fig. 43** Drogue parachute. Canopy skirt diameter during Stage 2 to 3 disreef

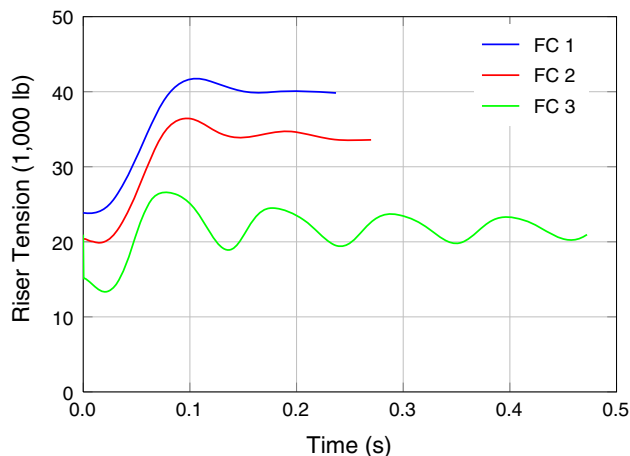


**Fig. 44** Drogue parachute. Riser tension during Stage 2 to 3 disreef

windows created by removing Sail 11 for every 5th gore. In FSI modeling of the MP parachute, the flow through the windows creates an additional challenge even for the fully-open parachutes, because the HMGP, introduced to deal with the flow through the hundreds of gaps and slits of spacecraft parachutes, cannot accurately model the flow through the windows. Therefore, in the case of the MP parachute, the challenges associated with the reefed stages and disreefing are compounded by the challenges associated with the need to resolve the flow through the windows. In this paper we have to a great extent overcome these formidable challenges in FSI modeling of spacecraft parachutes. We have successfully carried out, for a single parachute, FSI computation of both reefed stages and both disreefing events for both the MP and drogue parachutes. In the case of the MP parachute, we have also successfully carried out, for a 2-parachute cluster, FSI computation of the disreefing from Stage 2 to Stage 3.

**Acknowledgments** This work was supported in part by NASA Johnson Space Center Grant NNX13AD87G. It was also supported in part by the Rice–Waseda research agreement (first author).

## References

1. Takizawa K, Tezduyar TE (2012) Computational methods for parachute fluid-structure interactions. *Arch Comput Methods Eng* 19:125–169. doi:[10.1007/s11831-012-9070-4](https://doi.org/10.1007/s11831-012-9070-4)
2. Bazilevs Y, Takizawa K, Tezduyar TE (2013) *Computational fluid-structure interaction: methods and applications*. Wiley, Hoboken ISBN 978-0470978771
3. Takizawa K, Spielman T, Tezduyar TE (2011) Space-time FSI modeling and dynamical analysis of spacecraft parachutes and parachute clusters. *Comput Mech* 48:345–364. doi:[10.1007/s00466-011-0590-9](https://doi.org/10.1007/s00466-011-0590-9)
4. Takizawa K, Fritze M, Montes D, Spielman T, Tezduyar TE (2012) Fluid-structure interaction modeling of ringsail parachutes with disreefing and modified geometric porosity. *Comput Mech* 50:835–854. doi:[10.1007/s00466-012-0761-3](https://doi.org/10.1007/s00466-012-0761-3)
5. Takizawa K, Montes D, Fritze M, McIntyre S, Boben J, Tezduyar TE (2013) Methods for FSI modeling of spacecraft parachute dynamics and cover separation. *Math Models Methods Appl Sci* 23:307–338. doi:[10.1142/S0218202513400058](https://doi.org/10.1142/S0218202513400058)
6. Takizawa K, Tezduyar TE, Boben J, Kostov N, Boswell C, Buscher A (2013) Fluid-structure interaction modeling of clusters of spacecraft parachutes with modified geometric porosity. *Comput Mech* 52:1351–1364. doi:[10.1007/s00466-013-0880-5](https://doi.org/10.1007/s00466-013-0880-5)
7. Takizawa K, Tezduyar TE, Kolesar R, Kanai T (2014) FSI modeling of the Orion spacecraft drogue parachutes, in preparation
8. Tezduyar TE, Sathe S (2007) Modeling of fluid-structure interactions with the space-time finite elements: Solution techniques. *International Journal for Numerical Methods in Fluids* 54:855–900. doi:[10.1002/fld.1430](https://doi.org/10.1002/fld.1430)
9. Tezduyar TE (1992) Stabilized finite element formulations for incompressible flow computations. *Advances in Applied Mechanics* 28:1–44. doi:[10.1016/S0065-2156\(08\)70153-4](https://doi.org/10.1016/S0065-2156(08)70153-4)
10. Tezduyar TE, Behr M, Liou J (1992) A new strategy for finite element computations involving moving boundaries and interfaces – the deforming-spatial-domain/space-time procedure: I. The concept and the preliminary numerical tests. *Computer Methods in Applied Mechanics and Engineering* 94:339–351. doi:[10.1016/0045-7825\(92\)90059-S](https://doi.org/10.1016/0045-7825(92)90059-S)
11. Tezduyar TE, Behr M, Mittal S, Liou J (1992) A new strategy for finite element computations involving moving boundaries and interfaces—the deforming-spatial-domain/space-time procedure: II. Computation of free-surface flows, two-liquid flows, and flows with drifting cylinders. *Comput Methods Appl Mech Eng* 94:353–371. doi:[10.1016/0045-7825\(92\)90060-W](https://doi.org/10.1016/0045-7825(92)90060-W)
12. Tezduyar TE (2003) Computation of moving boundaries and interfaces and stabilization parameters. *Int J Numer Methods Fluids* 43:555–575. doi:[10.1002/fld.505](https://doi.org/10.1002/fld.505)
13. Takizawa K, Tezduyar TE (2011) Multiscale space-time fluid-structure interaction techniques. *Comput Mech* 48:247–267. doi:[10.1007/s00466-011-0571-z](https://doi.org/10.1007/s00466-011-0571-z)
14. Takizawa K, Tezduyar TE (2012) Space-time fluid-structure interaction methods. *Math Models Methods Appl Sci* 22:1230001. doi:[10.1142/S0218202512300013](https://doi.org/10.1142/S0218202512300013)
15. Brooks AN, Hughes TJR (1982) Streamline upwind/Petrov-Galerkin formulations for convection dominated flows with particular emphasis on the incompressible Navier-Stokes equations. *Comput Methods Appl Mech Eng* 32:199–259
16. Tezduyar TE, Mittal S, Ray SE, Shih R (1992) Incompressible flow computations with stabilized bilinear and linear equal-order



- interpolation velocity-pressure elements. *Comput Methods Appl Mech Eng* 95:221–242. doi:[10.1016/0045-7825\(92\)90141-6](https://doi.org/10.1016/0045-7825(92)90141-6)
17. Hughes TJR, Liu WK, Zimmermann TK (1981) Lagrangian-Eulerian finite element formulation for incompressible viscous flows. *Comput Methods Appl Mech Eng* 29:329–349
  18. Ohayon R (2001) Reduced symmetric models for modal analysis of internal structural-acoustic and hydroelastic-sloshing systems. *Comput Methods Appl Mech Eng* 190:3009–3019
  19. van Brummelen EH, de Borst R (2005) On the nonnormality of subiteration for a fluid-structure interaction problem. *SIAM J Sci Comput* 27:599–621
  20. Bazilevs Y, Calo VM, Zhang Y, Hughes TJR (2006) Isogeometric fluid-structure interaction analysis with applications to arterial blood flow. *Comput Mech* 38:310–322
  21. Khurram RA, Masud A (2006) A multiscale/stabilized formulation of the incompressible Navier-Stokes equations for moving boundary flows and fluid-structure interaction. *Comput Mech* 38:403–416
  22. Bazilevs Y, Calo VM, Hughes TJR, Zhang Y (2008) Isogeometric fluid-structure interaction: theory, algorithms, and computations. *Comput Mech* 43:3–37
  23. Dettmer WG, Peric D (2008) On the coupling between fluid flow and mesh motion in the modelling of fluid-structure interaction. *Comput Mech* 43:81–90
  24. Bazilevs Y, Gohean JR, Hughes TJR, Moser RD, Zhang Y (2009) Patient-specific isogeometric fluid-structure interaction analysis of thoracic aortic blood flow due to implantation of the Jarvik (2000) left ventricular assist device. *Comput Methods Appl Mech Eng* 198:3534–3550
  25. Bazilevs Y, Hsu M-C, Benson D, Sankaran S, Marsden A (2009) Computational fluid-structure interaction: methods and application to a total cavopulmonary connection. *Comput Mech* 45:77–89
  26. Bazilevs Y, Hsu M-C, Zhang Y, Wang W, Liang X, Kvamsdal T, Brekken R, Isaksen J (2010) A fully-coupled fluid-structure interaction simulation of cerebral aneurysms. *Comput Mech* 46:3–16
  27. Bazilevs Y, Hsu M-C, Zhang Y, Wang W, Kvamsdal T, Hentschel S, Isaksen J (2010) Computational fluid-structure interaction: methods and application to cerebral aneurysms. *Biomech Modell Mechanobiol* 9:481–498
  28. Bazilevs Y, Hsu M-C, Akkerman I, Wright S, Takizawa K, Henicke B, Spielman T, Tezduyar TE (2011) 3D simulation of wind turbine rotors at full scale. Part I: geometry modeling and aerodynamics. *Int J Numer Methods Fluids* 65:207–235. doi:[10.1002/fld.2400](https://doi.org/10.1002/fld.2400)
  29. Bazilevs Y, Hsu M-C, Kiendl J, Wüchner R, Bletzinger K-U (2011) 3D simulation of wind turbine rotors at full scale. Part II: fluid-structure interaction modeling with composite blades. *Int J Numer Methods Fluids* 65:236–253
  30. Akkerman I, Bazilevs Y, Kees CE, Farthing MW (2011) Isogeometric analysis of free-surface flow. *J Comput Phys* 230:4137–4152
  31. Hsu M-C, Bazilevs Y (2011) Blood vessel tissue prestress modeling for vascular fluid-structure interaction simulations. *Finite Elem Anal Design* 47:593–599
  32. Nagaoka S, Nakabayashi Y, Yagawa G, Kim YJ (2011) Accurate fluid-structure interaction computations using elements without mid-side nodes. *Comput Mech* 48:269–276. doi:[10.1007/s00466-011-0620-7](https://doi.org/10.1007/s00466-011-0620-7)
  33. Bazilevs Y, Hsu M-C, Takizawa K, Tezduyar TE (2012) ALE-VMS and ST-VMS methods for computer modeling of wind-turbine rotor aerodynamics and fluid-structure interaction. *Math Models Methods Appl Sci* 22:1230002. doi:[10.1142/S0218202512300025](https://doi.org/10.1142/S0218202512300025)
  34. Akkerman I, Bazilevs Y, Benson DJ, Farthing MW, Kees CE (2012) Free-surface flow and fluid-object interaction modeling with emphasis on ship hydrodynamics. *J Appl Mech* 79:010905
  35. Bazilevs Y, Hsu M-C, Scott MA (2012) Isogeometric fluid-structure interaction analysis with emphasis on non-matching discretizations, and with application to wind turbines. *Comput Methods Appl Mech Eng* 249–252:28–41
  36. Hsu M-C, Akkerman I, Bazilevs Y (2012) Wind turbine aerodynamics using ALE-VMS: validation and role of weakly enforced boundary conditions. *Comput Mech* 50:499–511
  37. Hsu M-C, Bazilevs Y (2012) Fluid-structure interaction modeling of wind turbines: simulating the full machine. *Comput Mech* 50:821–833
  38. Akkerman I, Dunaway J, Kvandal J, Spinks J, Bazilevs Y (2012) Toward free-surface modeling of planing vessels: simulation of the Fridsma hull using ALE-VMS. *Comput Mech* 50:719–727
  39. Minami S, Kawai H, Yoshimura S (2012) Parallel BDD-based monolithic approach for acoustic fluid-structure interaction. *Comput Mech* 50:707–718
  40. Miras T, Schotte J-S, Ohayon R (2012) Energy approach for static and linearized dynamic studies of elastic structures containing incompressible liquids with capillarity: a theoretical formulation. *Comput Mech* 50:729–741
  41. van Opstal TM, van Brummelen EH, de Borst R, Lewis MR (2012) A finite-element/boundary-element method for large-displacement fluid-structure interaction. *Comput Mech* 50:779–788
  42. Yao JY, Liu GR, Narmoneva DA, Hinton RB, Zhang Z-Q (2012) Immersed smoothed finite element method for fluid-structure interaction simulation of aortic valves. *Comput Mech* 50:789–804
  43. Laese A, Rossi R, Onate E, Idelsohn SR (2012) A coupled PFEM-Eulerian approach for the solution of porous FSI problems. *Comput Mech* 50:805–819
  44. Bazilevs Y, Takizawa K, Tezduyar TE (2013) Challenges and directions in computational fluid-structure interaction. *Math Models Methods Appl Sci* 23:215–221. doi:[10.1142/S0218202513400010](https://doi.org/10.1142/S0218202513400010)
  45. Bazilevs Y, Hsu M-C, Bement MT (2013) Adjoint-based control of fluid-structure interaction for computational steering applications. *Procedia Comput Sci* 18:1989–1998
  46. Korobenko A, Hsu M-C, Akkerman I, Tippmann J, Bazilevs Y (2013) Structural mechanics modeling and FSI simulation of wind turbines. *Math Models Methods Appl Sci* 23:249–272
  47. Korobenko A, Hsu M-C, Akkerman I, Bazilevs Y (2013) Aerodynamic simulation of vertical-axis wind turbines. *J Appl Mech* 81:021011. doi:[10.1115/1.4024415](https://doi.org/10.1115/1.4024415)
  48. Bazilevs Y, Korobenko A, Deng X, Yan J, Kinzel M, Dabiri JO (2014) FSI modeling of vertical-axis wind turbines. *J Appl Mech*, published online, doi:[10.1115/1.4027466](https://doi.org/10.1115/1.4027466)
  49. Yao JY, Liu GR, Qian D, Chen CL, Xu GX (2013) A moving-mesh gradient smoothing method for compressible CFD problems. *Math Models Methods Appl Sci* 23:273–305
  50. Kamran K, Rossi R, Onate E, Idelsohn SR (2013) A compressible Lagrangian framework for modeling the fluid-structure interaction in the underwater implosion of an aluminum cylinder. *Math Models Methods Appl Sci* 23:339–367
  51. Hsu M-C, Akkerman I, Bazilevs Y (2014) Finite element simulation of wind turbine aerodynamics: validation study using NREL Phase VI experiment. *Wind Energy* 17:461–481
  52. Long CC, Marsden AL, Bazilevs Y (2013) Fluid-structure interaction simulation of pulsatile ventricular assist devices. *Comput Mech* 52:971–981. doi:[10.1007/s00466-013-0858-3](https://doi.org/10.1007/s00466-013-0858-3)
  53. Long CC, Esmaily-Moghadam M, Marsden AL, Bazilevs Y (2013) Computation of residence time in the simulation of pulsatile ventricular assist devices. *Computational Mechanics*, published online, September 2013, doi:[10.1007/s00466-013-0931-y](https://doi.org/10.1007/s00466-013-0931-y)
  54. Yao J, Liu GR (2014) A matrix-form GSM-CFD solver for incompressible fluids and its application to hemodynamics. *Computational Mechanics*, published online, February 2014, doi:[10.1007/s00466-014-0990-8](https://doi.org/10.1007/s00466-014-0990-8)
  55. Long CC, Marsden AL, Bazilevs Y (2014) Shape optimization of pulsatile ventricular assist devices using FSI to minimize throm-

- botic risk, *Computational Mechanics*, published online, January 2014, doi:[10.1007/s00466-013-0967-z](https://doi.org/10.1007/s00466-013-0967-z)
56. Tezduyar TE, Sathe S, Pausewang J, Schwaab M, Christopher J, Crabtree J (2008) Interface projection techniques for fluid-structure interaction modeling with moving-mesh methods. *Comput Mech* 43:39–49. doi:[10.1007/s00466-008-0261-7](https://doi.org/10.1007/s00466-008-0261-7)
  57. Tezduyar TE, Sathe S, Schwaab M, Pausewang J, Christopher J, Crabtree J (2008) Fluid-structure interaction modeling of ringsail parachutes. *Comput Mech* 43:133–142. doi:[10.1007/s00466-008-0260-8](https://doi.org/10.1007/s00466-008-0260-8)
  58. Tezduyar TE, Takizawa K, Moorman C, Wright S, Christopher J (2010) Space-time finite element computation of complex fluid-structure interactions. *Int J Numer Methods Fluids* 64:1201–1218. doi:[10.1002/fld.2221](https://doi.org/10.1002/fld.2221)
  59. Takizawa K, Moorman C, Wright S, Spielman T, Tezduyar TE (2011) Fluid-structure interaction modeling and performance analysis of the Orion spacecraft parachutes. *Int J Numer Methods Fluids* 65:271–285. doi:[10.1002/fld.2348](https://doi.org/10.1002/fld.2348)
  60. Takizawa K, Wright S, Moorman C, Tezduyar TE (2011) Fluid-structure interaction modeling of parachute clusters. *Int J Numer Methods Fluids* 65:286–307. doi:[10.1002/fld.2359](https://doi.org/10.1002/fld.2359)
  61. Takizawa K, Spielman T, Moorman C, Tezduyar TE (2012) Fluid-structure interaction modeling of spacecraft parachutes for simulation-based design. *J Appl Mech* 79:010907. doi:[10.1115/1.4005070](https://doi.org/10.1115/1.4005070)
  62. Chung J, Hulbert GM (1993) A time integration algorithm for structural dynamics with improved numerical dissipation: The generalized- $\alpha$  method. *J Appl Mech* 60:371–375